Clin Orthop Relat Res (2017) 475:3026–3043
DOI 10.1007/s11999-017-5486-3

Clinical Orthopaedics and Related Research®
A Publication of The Association of Bone and Joint Surgeons®

CLINICAL RESEARCH

Alloy Microstructure Dictates Corrosion Modes in THA Modular Junctions

Robin Pourzal PhD, Deborah J. Hall BS, Jonas Ehrich BS, Stephanie M. McCarthy BS, Mathew T. Mathew PhD, Joshua J. Jacobs MD, Robert M. Urban

Received: 1 December 2016 / Accepted: 28 August 2017 / Published online: 7 September 2017

Abstract

Background Adverse local tissue reactions (ALTRs) triggered by corrosion products from modular taper junctions are a known cause of premature THA failure. CoCrMo devices are of particular concern because cobalt ions and chromium-orthophosphates were shown to be linked to ALTRs, even in metal-on-polyethylene THAs. The most common categories of CoCrMo alloy are cast and wrought alloy, which exhibit fundamental microstructural differences in terms of grain size and hard phases. The impact of implant alloy microstructure on the occurring modes of corrosion and subsequent metal ion release is not well understood.

Questions/purposes The purpose of this study was to determine whether (1) the microstructure of cast CoCrMo alloy varies broadly between manufacturers and can dictate specific corrosion modes; and whether (2) the microstructure of wrought CoCrMo alloy is more consistent between manufacturers and has low implications on the alloy's corrosion behavior.

Methods The alloy microstructure of four femoral-stem and three femoral-head designs from four manufacturers was metallographically and electrochemically characterized. Three stem designs were made from cast alloy; all three head designs and one stem design were made from

Rush University Medical Center has received funding from the National Institutes of Health/National Institute of Arthritis and Musculoskeletal and Skin Diseases (R01 AR070181; RP), the Rush Translational Science Consortium (RP), and the Rush Arthritis and Orthopedic Institute (RMU). Two of the authors (DJH, RMU) received research funding partially related to the submitted work and two authors (DJH, JJJ) received research funding outside the submitted work from Zimmer Inc (Warsaw, IN, USA). One of the authors (JJJ) received research funding outside the submitted work from Nu-Vasive (San Diego, CA, USA) and Medtronics (Memphis, TN, USA). Two authors (DJH, RMU) were paid consultants outside the submitted work for Wright Medical Technology (Memphis, TN, USA) and AgNovos Healthcare (New York, NY, USA). One of the authors (RMU) was a paid consultant outside the submitted work for Exactech (Gainesville, FL, USA), Intrinsic Therapeutics (Woburn, MA, USA), AgNovos Healthcare, DePuy Synthes (New Brunswick, NJ, USA), Spinal Motion (Fairfax, VA, USA), and Zimmer Inc. One author (JJJ) has stocks/stock options in Implant Protection (Raanana, Israel).
All ICMJE Conflict of Interest Forms for authors and *Clinical Orthopaedics and Related Research*® editors and board members are on file with the publication and can be viewed on request.
Clinical Orthopaedics and Related Research® neither advocates nor endorses the use of any treatment, drug, or device. Readers are encouraged to always seek additional information, including FDA-approval status, of any drug or device prior to clinical use.

Each author certifies that his or her institution approved the human protocol for this investigation and that all investigations were conducted in conformity with ethical principles of research.
This work was performed at Rush University Medical Center, Chicago, IL, USA.

Electronic supplementary material The online version of this article (doi:10.1007/s11999-017-5486-3) contains supplementary material, which is available to authorized users.

R. Pourzal (✉), D. J. Hall, J. Ehrich, S. M. McCarthy, J. J. Jacobs, R. M. Urban
Department of Orthopedic Surgery, Rush University Medical Center, 1611 W Harrison Street, Suite 204-H, Chicago, IL 60612, USA
e-mail: robin_pourzal@rush.edu

J. Ehrich
Institut für Technologien der Metalle, Werkstofftechnik, University of Duisburg-Essen, Duisburg, Germany

M. T. Mathew
Department of Biomedical Sciences, University of Illinois Medical College at Rockford, Rockford, IL, USA

wrought alloy. Alloy samples were sectioned from retrieved components and then polished and etched to visualize grain structure and hard phases such as carbides (eg, $M_{23}C_6$) or intermetallic phases (eg, σ phase). Potentiodynamic polarization (PDP) tests were conducted to determine the corrosion potential (E_{corr}), corrosion current density (I_{corr}), and pitting potential (E_{pit}) for each alloy. Four devices were tested within each group, and each measurement was repeated three times to ensure repeatable results. Differences in PDP metrics between manufacturers and between alloys with different hard phase contents were compared using one-way analysis of variance and independent-sample t-tests. Microstructural features such as twin boundaries and slip bands as well as corrosion damage features were viewed and qualitatively assessed in a scanning electron microscope.

Results We found broad variability in implant alloy microstructure for both cast and wrought alloy between manufacturers, but also within the same implant design. In cast alloys, there was no difference in PDP metrics between manufacturers. However, coarse hard phases and clusters of hard phases (mainly intermetallic phases) were associated with severe phase boundary corrosion and pitting corrosion. Furthermore, cast alloys with hard phases had a lower E_{pit} than those without (0.46 V, SD 0.042; 0.53 V, SD 0.03, respectively; $p = 0.015$). Wrought alloys exhibited either no hard phases or numerous carbides ($M_{23}C_6$). However, the corrosion behavior was mainly affected by lattice defects and banded structures indicative of segregations that appear to be introduced during bar stock manufacturing. Alloys with banding had a lower E_{corr} ($p = 0.008$) and higher I_{corr} ($p = 0.028$) than alloys without banding (−0.76 V, SD 0.003; −0.73 V, SD 0.009; and 1.14×10^{-4} mA/cm^2, SD 1.47×10^{-5}; 5.2×10^{-5} mA/cm^2, SD 2.57×10^{-5}, respectively). Alloys with carbides had a slightly higher E_{corr} ($p = 0.046$) than those without (−0.755 V, SD 0.005; −0.761 V, SD 0.004); however, alloys with carbides exhibited more severe corrosion damage as a result of phase boundary corrosion, hard phase detachment, and subsequent local crevice corrosion.

Conclusions The observed variability in CoCrMo alloy microstructure of both cast and wrought components in this study appears to be an important issue to address, perhaps through better standards, to minimize in vivo corrosion. The finding of the banded structures within wrought alloys is especially concerning because it unfavorably influences the corrosion behavior independent of the manufacturer. The findings suggest that a homogeneous alloy microstructure with a minimal hard phase fraction exhibits more favorable corrosion behavior within the in vivo environment of modular taper junctions, thus lowering metal ion release and subsequently the risk of ALTRs to corrosion products. Also, the question arises if hard phases fulfill a useful purpose in metal-on-polyethylene bearings, because they may come with a higher risk of phase boundary corrosion and pitting corrosion and the benefit they provide by adding strength is not needed (unlike in metal-on-metal bearings).

Clinical Relevance Implant failure resulting from corrosion processes within modular junctions is a major concern in THA. Our results suggest that implant alloy microstructure is not sufficiently standardized and may also dictate specific corrosion modes and subsequent metal ion release.

Introduction

The release of corrosion products from modular taper junctions in THAs has been a longstanding subject of research in the orthopaedic research community [7, 10, 14, 22]. Recently, awareness of the possibly detrimental consequences of adverse local tissue reactions (ALTRs) to corrosion products has increased [35, 40, 50]. Initially, concern was mainly targeted on metal-on-metal devices; however, several studies have shown that ALTRs can also occur in metal-on-polyethylene and even ceramic-on-polyethylene bearings [11, 29, 45] in which there was corrosion of the modular junction. Of greatest concern are corrosion products generated from CoCrMo alloy, where it has been shown that cobalt can be especially detrimental at elevated concentrations [8, 27]. Histopathologically, ALTRs are often associated with the accumulation of lymphocytes in the presence of chromium phosphate particles [18, 22], yet the concept of modularity and the use of CoCrMo alloys bear considerable advantages. Modularity provides the surgeon with valuable flexibility during surgery. CoCrMo alloys bear a lower risk of fatigue fracture than titanium alloy alternatives [38]. It is also important to note that most implants perform well clinically. For example, our own retrieval analysis of > 300 implants has shown that 85% of CoCrMo stem and head tapers exhibited none to minimal visual evidence of corrosion at an average time in vivo of 5 years, whereas only 6% exhibited severe corrosion [20]. However, considering the large number of THAs implanted per year [26], the rising incidence of ALTR-related premature implant failures [35, 40, 50], and the devastating disability that patients with ALTRs can be afflicted with, it is important to better understand the corrosion pathways to determine appropriate countermeasures.

The damage mode occurring within modular junctions has been most commonly described as mechanically assisted crevice corrosion (MACC) [17]. However, implant retrieval analysis has revealed many underlying damage modes. The most commonly studied damage mode is fretting corrosion, where damage is initiated by micromotion, leading to passive film disruption and subsequent

tribocorrosive processes [7, 13]. Other damage modes such as etching, pitting, grain, and phase boundary corrosion also occur frequently (Fig. 1A–C), but have not been given as much attention [14, 20, 22]. Recently, other damage pathways such as proximal-distal running etched troughs on head taper surfaces (column damage; Fig. 1D) [10, 20, 25], imprinting of the stem topography into the head taper surface [5, 48], and cell-induced corrosion processes [16, 20] have also been described.

There are two common CoCrMo alloy types: cast (ASTM F75) [2] and wrought (ASTM F1537) [3] alloy. Both materials are used for THAs. Although the chemical composition and mechanical properties of both cast and wrought alloys are standardized, the implant alloy microstructure is not constrained by any standard and can vary broadly in terms of grain size, hard phase types and size as well as hard phase volume fraction. Especially for cast alloy, the microstructure is highly dependent on the manufacturing process, subsequent type of heat treatment, and implant geometry [6, 36, 49], whereas wrought alloy is more homogeneous as a result of thermomechanical processing of the bar stock material [4, 30]. It is important to note that some damage modes—such as etching, grain, and phase boundary—appear to be inherently linked to implant microstructure [19, 20, 39].

Therefore, it was the purpose of this study to determine whether (1) the microstructure of cast CoCrMo alloy varies broadly between manufacturers and can dictate specific corrosion modes; and whether (2) the microstructure of wrought CoCrMo alloy is more consistent between manufacturers and has low implications on the alloy's corrosion behavior.

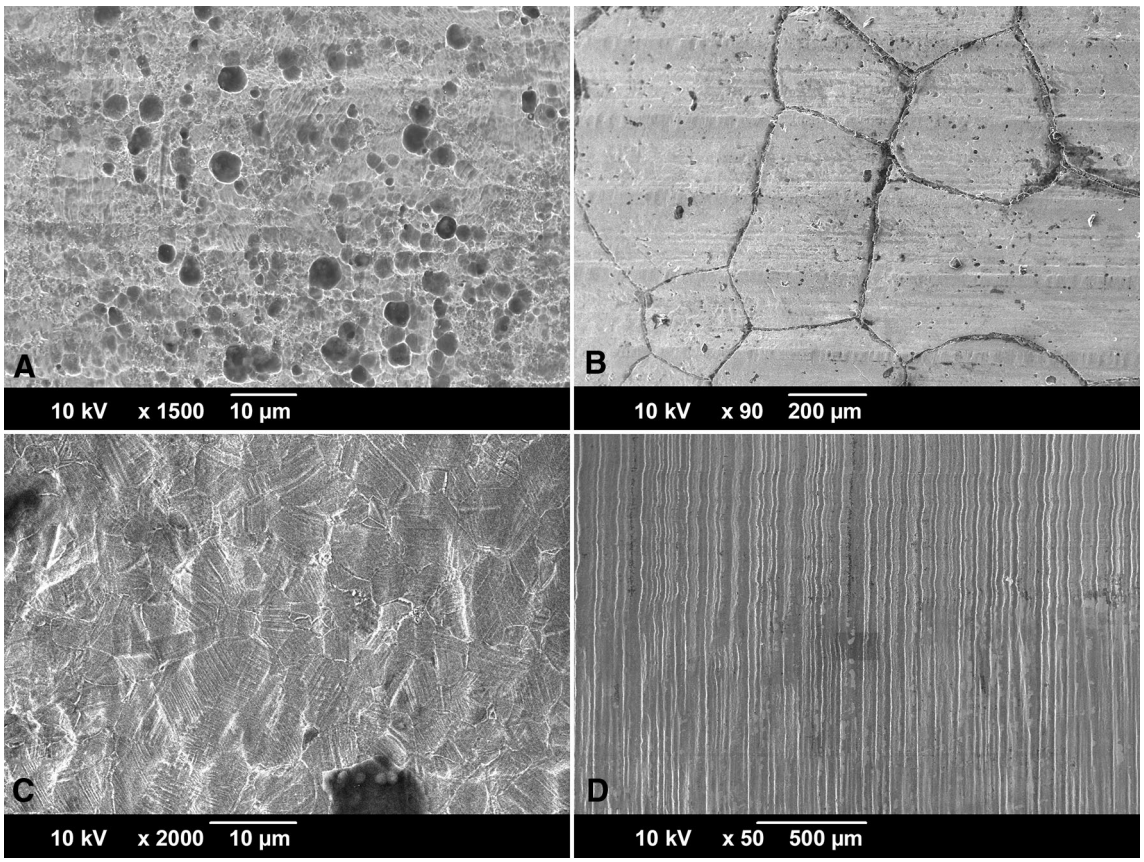

Fig. 1A–D SEM micrographs of frequently in vivo occurring damage modes on surgically retrieved stem (**A**–**B**) and head tapers (**C**–**D**). (**A**) Pitting corrosion is caused by a local chemical imbalance and is characterized by round pits. Here it is shown on a cast alloy stem, but it can also occur on wrought alloy. (**B**) Intergranular corrosion occurs most dominantly on cast alloy and is characterized by complete dissolution of the grain boundaries followed by local crevice corrosion. (**C**) Etching is a more uniform corrosion process of entire grains, where the dissolution rate depends on crystal orientation, residual stresses, and lattice defects. Etching occurs on both cast and wrought alloys but is more prominently visible on wrought alloy—as shown here—resulting from the smaller grain size and twin density. (**D**) Column damage occurs only in wrought alloy femoral heads and is characterized by long column-like troughs running perpendicular to the initial taper topography in the proximal-distal direction.

Materials and Methods

For this study, only CoCrMo components from modular metal-on-polyethylene THAs were included. In total, 209 femoral stems and 776 femoral heads were available from an institutional review board-approved implant repository. All stems and heads had 12/14-type tapers. Damage caused to the taper surfaces in vivo was scored using a modified Goldberg score with combined corrosion and fretting score [17]. The damage was scored from least to most severe as minimal (1), mild (2), moderate (3), or severe (4). Two observers scored the surfaces (RMU, DJH). In the case of disagreement in scores between the two observers, the observers discussed and came to a consensus on the score. The reliability of this method has recently been demonstrated [21]. For the corrosion tests, stems of four different THA designs made by four different manufacturers were chosen. In alphabetical order, the manufacturers were DePuy Synthes, Solutions (Warsaw, IN, USA), Smith & Nephew, Echelon (Memphis, TN, USA), Stryker, Definition (Kalamazoo, MI, USA), and Zimmer Biomet, VerSys Beaded Fullcoat (Warsaw, IN, USA). All femoral stems were made from cast CoCrMo alloy (Table 1) except for one that was made from wrought alloy (Table 2). Eight femoral stems were primary components and six were revision components. Twelve femoral stems were implanted as cementless components and two were fixed using cement. Three different femoral heads made by different manufacturers (DePuy Synthes, Stryker, and Zimmer Biomet) were also tested (Table 2). All heads were made from wrought CoCrMo alloy. The samples will be referred to as stem alloy 1–4 (SA 1–4) and head alloy 1–3 (HA 1–3). In this study, we are not identifying the manufacturer of

Table 1. Overview of cast alloy samples*

Implant design	Sample number	Time in situ (months)	Taper type	Damage score	Alloy type
SA-1	SA-1-1	127.6	12/14	1	1
	SA-1-2	48.5	12/14	3	2
	SA-1-3	49.5	12/14	4	1
	SA-1-4	83.1	12/14	4	1
SA-2	SA-2-1	11.6	12/14	1	2
	SA-2-2	1.0	12/14	1	2
	SA-2-3	5.9	12/14	1	2
	SA-2-4	89.9	12/14	3	2
SA-3	SA-3-1	37.7	12/14	1	2
	SA-3-2	112.5	12/14	1	2
	SA-3-3	122.1	12/14	3	1
	SA-3-4	129.9	12/14	2	2

* Alloys came from three stem designs made by three different manufacturers (SA-1, SA-2, and SA-3); there were four components per design (eg, SA-1-1, SA-1-2, etc); the damage score was a modified Goldberg score [12]; alloy type refers to alloys with a hard phase volume fraction of < 1% (Type 1) or 1%–5% (Type 2).

Table 2. Overview of wrought alloy samples*

Implant design	Sample number	Time in situ (months)	Head size (mm)	Taper type	Damage score	Column damage	Alloy type	Banded structure
HA-1	HA-1-1	122.1	28	12/14	1	N	2	N
	HA-1-2	29.8	36	12/14	4	N	2	N
	HA-1-3	16.7	32	12/14	4	N	1	Y
	HA-1-4	176.8	32	12/14	4	Y	2	Y
HA-2	HA-2-1	31.4	36	12/14	4	Y	1	Y
	HA-2-2	53.9	36	12/14	3	N	1	Y
	HA-2-3	84	36	12/14	1	N	2	Y
	HA-2-4	77	32	12/14	4	Y	2	Y
HA-3	HA-3-1	1.1	32	12/14	4	Y	2	Y
	HA-3-2	83.1	32	12/14	4	Y	2	Y
	HA-3-3	24.5	32	12/14	4	Y	1	Y
	HA-3-4	60.8	40	12/14	1	N	1	Y
	HA-3-5	98.9	28	12/14	1	N	1	Y
SA-4	SA-4-1	111.3	–	12/14	3	N	2	N
	SA-4-2	NA	–	12/14	4	N	2	N

* Alloys came from three head designs and one stem design made by three different manufacturers (HA-1, HA-2, HA-3, and SA-4); there were four components for HA-1 and HA-2, five components for HA-3, and two components for SA-4; the damage score was a modified Goldberg score [12]; alloy type refers to alloys with a hard phase volume fraction of < 1% (Type 1) or 1% to 5% (Type 2); N = no; Y = yes; NA = not available.

specific samples because of the small number of components analyzed. There were at least four components for each implant design. For each implant type, at least one component with minimal to mild corrosion damage and one with moderate to severe corrosion damage were included. The only exception was SA-4 for which only two components were available that had moderate and severe corrosion damage. For the metallographic evaluation and corrosion tests, stem samples were sectioned perpendicular (transverse) to the taper axis and distally from the stem taper (Fig. 2A). Head-taper samples were sectioned from the bulk material of the head in the longitudinal direction parallel to the head-taper axis (Fig. 2B) using a cutoff saw with abrasive wheels. Alloy samples were embedded in two ways: (1) in epoxy for metallographic evaluation; and (2) in a conductive epoxy resin for corrosion tests. Samples were ground (320 grit) and polished sequentially with 9-, 3-, and 1-µm diamond suspension to generate a new surface with no prior exposure to the in vivo environment. The resulting average roughness was Ra < 0.03 µm. Metal alloys in most technical applications are polycrystalline, which means that they consist of multiple crystals, or grains, with different crystal orientations. The average diameter of the crystals—known as grain size—can vary broadly depending on the thermal and mechanical treatment of the alloy. Metallographic etching was performed to visualize the grain structure of the alloy samples. An etchant composed of 50 mL HCl, 50 mL water, and 4 g potassium-bisulfate was chosen [42]. For an optimal etching process, the alloy samples were immersed into the etchant for up to 40 seconds. After the etching process, the grain structure was observed using a light or scanning electron microscope. Besides the evaluation of the grain size, light microscopic images of etched samples may reveal any inhomogeneity of the alloy's microstructure such as banding. Also, other microstructural features such as slip bands (parallel, step-like features indicative of local deformation and lattice defects) or twin boundaries (parallel lines within grains, common in austenitic alloys) were observed. Another important microstructural feature in CoCrMo alloys is hard phases. Hard phases are second phases embedded within the solid solution matrix of CoCrMo alloy and are harder than the matrix itself [28]. Such hard phases can either be carbides or intermetallic phases. Carbides consist of a metal in combination with carbon and can occur in different modifications such as $M_{23}C_6$, M_7C_3, and M_6C (M = metal, typically chromium or molybdenum in CoCrMo alloy) [24, 28, 37, 42]. Intermetallic phases consist of different combinations of typically two metals (eg, Cr_xCo_x, Co_xMo_x) and are not dissolved within the solid solution. The presence of silicon typically enhances the formation of intermetallic phases. In CoCrMo alloy, intermetallic phases such as σ- and µ-phase have been shown to occur [24, 37, 46]. For the evaluation of the hard phase volume fraction, polished alloy samples were etched for 10 seconds in a solution of 43 g potassium manganate and 22.5 g potassium hydroxide in 200 mL of distilled water. This etching procedure resulted in dark staining of hard phases, which were then analyzed with a light microscope at × 500. Here, only two types of alloys were distinguished: Type 1 had little to no hard phases (< 1%), and Type 2 had an obvious hard phase volume fraction of 1%–5%. The etched images were evaluated by two observers (RP, JE). Corrosion tests were performed in a corrosion cell with a standard three-electrode setup with a graphite counterelectrode and a saturated calomel electrode (SCE) as a reference electrode (Fig. 2C). The alloy sample was mounted in a way that only the alloy itself was exposed to the testing fluid. An O-ring ensured that a constant surface area of 0.38 cm^2 was exposed to the testing fluid, whereas the conductive resin was isolated and

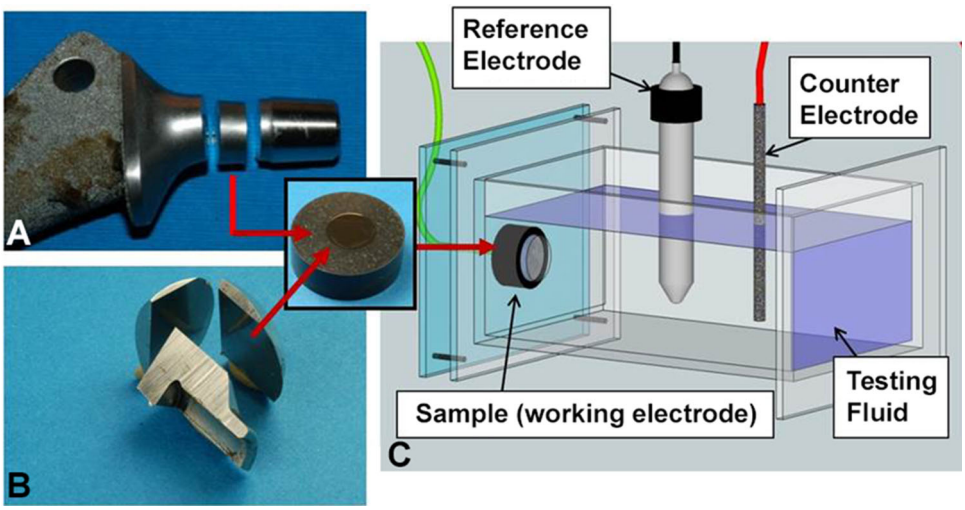

Fig. 2A–C Sectioned stem (**A**) and head (**B**) illustrating the alloy sampling location for corrosion tests; (**C**) schematic of the setup for the cyclic PDP tests.

not exposed to the fluid. A sequence of standard electrochemical tests was performed including a cathodic sweep, the open circuit potential, and cyclic potentiodynamic polarization (PDP) (−0.8 to 1.8 V versus SCE, scan rate of 2 mV/s) [32, 33]. All tests were conducted at 37° C in simulated joint fluid (newborn calf serum, Tris-buffered) with a protein concentration of 30 g/L. From the polarization curves, the corrosion potential (E_{corr}), the corrosion current density (I_{corr}), and the pitting potential (E_{pit}) were estimated by using Tafel's slope method (Fig. 3) [34]. The E_{pit} was determined from the cathodic scan of the potential loop. E_{corr} is indicative of the corrosion tendency, I_{corr} is a measure of the corrosion rate, and E_{pit} is indicative of the alloy's pitting behavior (Table 3). All alloy samples were tested in triplicate. For a single implant, the results showed repeatable results for all metrics. Differences in E_{corr}, I_{corr}, and E_{pit}, between alloys of different categories (cast, wrought), from different manufacturers, or with different microstructural features were tested with one-way analysis of variance and independent-sample t-tests. After the corrosion tests, samples were viewed in a scanning electron microscope (SEM) (JSM-6490LV; JEOL, Peabody, MA, USA) to visualize damage patterns and how they relate to microstructural features. Chemical composition of hard phases was analyzed using energy dispersive x-ray spectroscopy (EDS) and in some cases imaged with the backscattered electron mode (BSE) in the SEM. It is important to note that PDP tests do not simulate the exact electrochemical conditions that occur in vivo. Its primary function is to determine the basic corrosion behavior of an alloy within a specific testing fluid. However, as a result of the nature of the test, electrochemically induced damage features will occur [33], which can be indicative of specific corrosion modes.

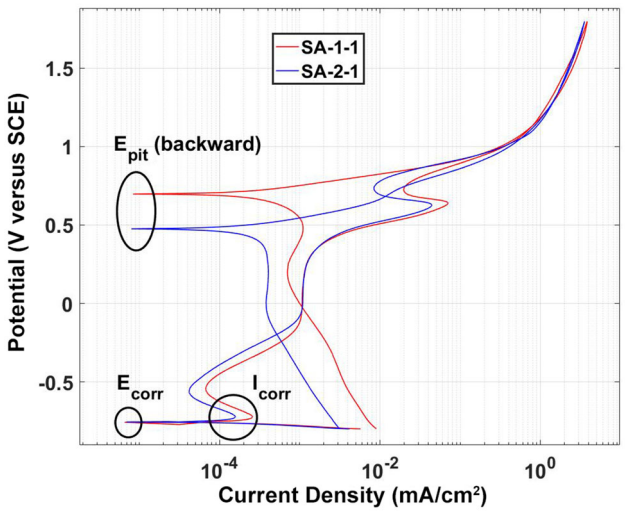

Fig. 3 Example PDP curves from two different alloys (SA-1-1 and SA-2-1). Here the two alloys have similar E_{corr} and I_{corr} but a distinctively different E_{pit}.

Results

Within the cast alloy samples, the smallest grain size range was found in stem design SA-1 with 200–500 μm followed by SA-2 with 0.3–1 mm and SA-3 with 0.5–1.5 mm (Fig. 4). Grain size could be visualized through etching; however, the clearest visualization of microstructural features was achieved during the corrosion tests resulting from the common occurrence of grain boundary corrosion in all alloys (Fig. 4). After cyclic polarization (PDP tests), SA-1 often exhibited areas covered with chromium oxide films (Fig. 5A). In most cases, there were very few pits and little evidence of hard phases within the alloy microstructure (Fig. 5B). Only in one case (SA-1-4) were clusters of fine hard phases observed. SA-2 exhibited mostly clusters of fine hard phases, which were rich in Mo and Si (Appendix 1 [Supplemental materials are available with the online version of *CORR*®.]) and were either round or elongated in shape. Such hard phase clusters were strongly associated with pitting (Fig. 5C). In three cases, there were also coarse mixed hard phases located on the grain boundaries consisting of at least two different hard phases, which were most likely intermetallic as a result of the lack of carbon (Fig. 5D; Appendix 1). Such hard phases were usually surrounded by deep trenches caused by phase boundary corrosion and appeared in some cases to have completely

Table 3. Explanation of metrics derived from cyclic potentiodynamic polarization (PDP) curves (Fig. 3)*

PDP metric	Symbol	Unit	Explanation
Corrosion potential	E_{corr}	V (versus SCE)	Measure of an alloy's overall corrosion tendency; under equal conditions, a higher E_{corr} indicates a lower corrosion tendency
Corrosion current density	I_{corr}	mA/cm^2	Measure of an alloy's corrosion rate; under equal conditions, a higher I_{corr} is directly related to a higher metal ion release rate
Pitting potential	E_{pit}	V (versus SCE)	The pitting potential is an indicator of an alloy's receptivity for pitting corrosion; under equal conditions, a higher E_{pit} indicates better protection of pitting corrosion

* E_{corr} and E_{pit} are measured relative to the reference electrode (saturated calomel electrode [SCE]).

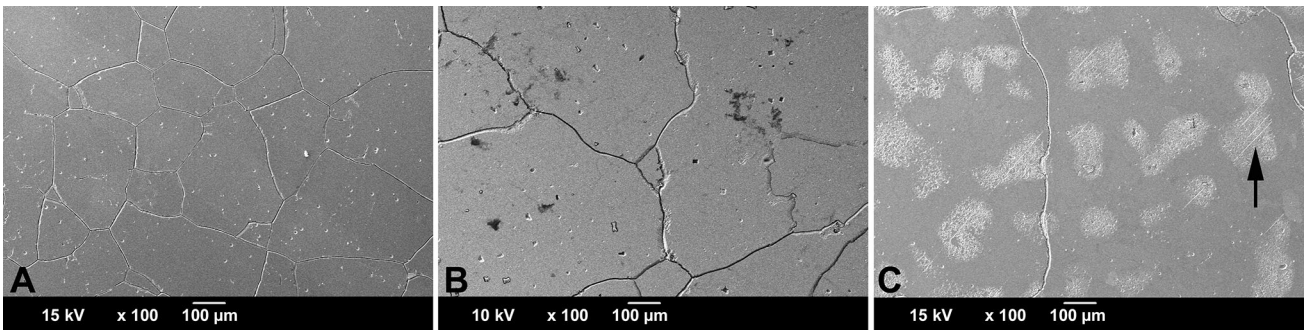

Fig. 4A–C All alloys exhibited intergranular corrosion after corrosion tests, thus visualizing varying grain size: (**A**) SA-1 exhibited a grain size of 200–500 µm and only few randomly distributed pits; (**B**) SA-2 had a grain size range of 0.3–1 mm and exhibited pits locally; (**C**) SA-3 had a coarse grain size of 0.5–1.5 mm and exhibited a homogeneous distribution of areas with severe pitting (arrow).

detached leaving fine round or elongated pits (Fig. 5E) and broad shallow pits along the grain boundaries (Fig. 5F). SA-3 was the most inconsistent alloy. It appeared to have a varying concentration of coarse hard phases located within a large grain, and one case exhibited no hard phases at all. When present, hard phases appeared to be carbidic as evidenced by a strong EDS carbon signal with some Mo- and Si-rich areas (Fig. 5G). These coarse hard phases were usually surrounded by numerous finer phases (< 500 nm) (Fig. 5H), which were associated with severe pitting leading to patches of marked corrosion within the grains (Figs. 4C, 5G; Appendix 1). With respect to the PDP metrics, the mean E_{corr} was −0.751 V (SD 0.005; 95% confidence interval [CI], −0.759 to −0.742), −0.755 V (SD 0.004; 95% CI, −0.762 to −0.748), and −0.755 V (SD 0.005; 95% CI, −0.763 to −0.748) for SA-1, SA-2, and SA-3, respectively. The I_{corr} and E_{pit} values were 7.46×10^{-4} mA/cm^2 (SD 1.37×10^{-4}; 95% CI, 5.28×10^{-4} to 9.64×10^{-4}), 3.56×10^{-4} mA/cm^2 (SD 2.73×10^{-4}; 95% CI, 0–7.90×10^{-4}), and 6.24×10^{-4} mA/cm^2 (SD 4.69×10^{-4}; 95% CI, 0–1.37×10^{-4}) and 0.505 V (SD 0.035; 95% CI, 0.45–0.561), 0.469 V (SD 0.027; 95% CI, 0.425–0.512), and 0.486 V (SD 0.08; 95% CI, 0.359–0.613), respectively (Table 4). There was no difference in E_{corr} ($p = 0.41$), I_{corr} ($p = 0.27$), or E_{pit} ($p = 0.63$) among the three manufacturers with the numbers available (Fig. 6). There was considerable variability within corrosion current density and pitting potential for some alloys, especially regarding the corrosion current for SA-2 and SA-3 and the pitting potential of SA-3, which also exhibited a variation in hard phase content. For further comparison, all samples were regrouped by the presence or absence of hard phases independent of the manufacturer. Alloys without hard phases that were visible under the SEM or with only minimal amounts of single randomly distributed hard phases were categorized as Type 1 cast alloy, and those with a prominent occurrence of any type and size of hard phases were categorized as Type 2 cast alloy (Table 1). The E_{corr} and I_{corr} were −0.751 V (SD 0.005; 95% CI, −0.759 to −0.741) and −0.756 V (SD 0.004; 95% CI, −0.759 to −0.753) (Fig. 7A) and 5.99×10^{-4} mA/cm^2 (SD 3.61×10^{-4}; 95% CI, 2.48×10^{-5} to 1.17×10^{-3}) and 5.64×10^{-4} mA/cm^2 (SD 3.51×10^{-4}; 95% CI, 2.70×10^{-4} to 8.57×10^{-4}) (Fig. 7B) for Types 1 and 2, respectively. There was no difference in E_{corr} ($p = 0.13$) or I_{corr} ($p = 0.88$) between alloy types (Fig. 7). However, Type 1 alloy had a higher ($p = 0.015$) E_{pit} (0.533 V, SD 0.03 V; 95% CI, 0.486–0.58) than Type 2 alloy (0.464 V, SD 0.042; 95% CI, 0.429–0.499) (Fig. 7C). Type 2 cast alloy was further distinguished into three subtypes: Type 2a had some areas with fine hard phase clusters, Type 2b had mixed hard phases along the grain boundaries with fine hard phase clusters, and Type 2c had coarse hard phases surrounded by fine hard phase clusters within the grains. With regard to E_{pit}, Types 2b (0.452 V, SD 0.05; 95% CI, 0.378–0.527) and 2c (0.455 V, SD 0.03; 95% CI, 0.202–0.708) had a lower E_{pit} ($p = 0.028$, $p = 0.038$, respectively) than Type 1, whereas Type 2a exhibited no difference ($p = 0.27$) with the available sample size (Fig. 7D). There was also no difference in taper score ($p = 0.78$, Mann-Whitney U) between head tapers with Type 1 (median, 2.0; range, 1–4) or Type 2 (median, 1.5; range 1–4) cast alloy microstructure.

The light microscopic analysis of the head wrought alloys further revealed that all but two samples (HA-1-1, HA-1-2) exhibited a banded structure in the longitudinal direction parallel to the taper axis (Fig. 8), whereas samples prepared in the transverse direction had no such pattern (Table 2). In the transverse direction, samples with longitudinal banding would also exhibit residual dendritic features that remained from the initial cast process of the alloy (Fig. 8B). The two available samples of SA-4, prepared perpendicular to the stem taper axis, did not exhibit the banded pattern. All head alloys exhibited a comparable

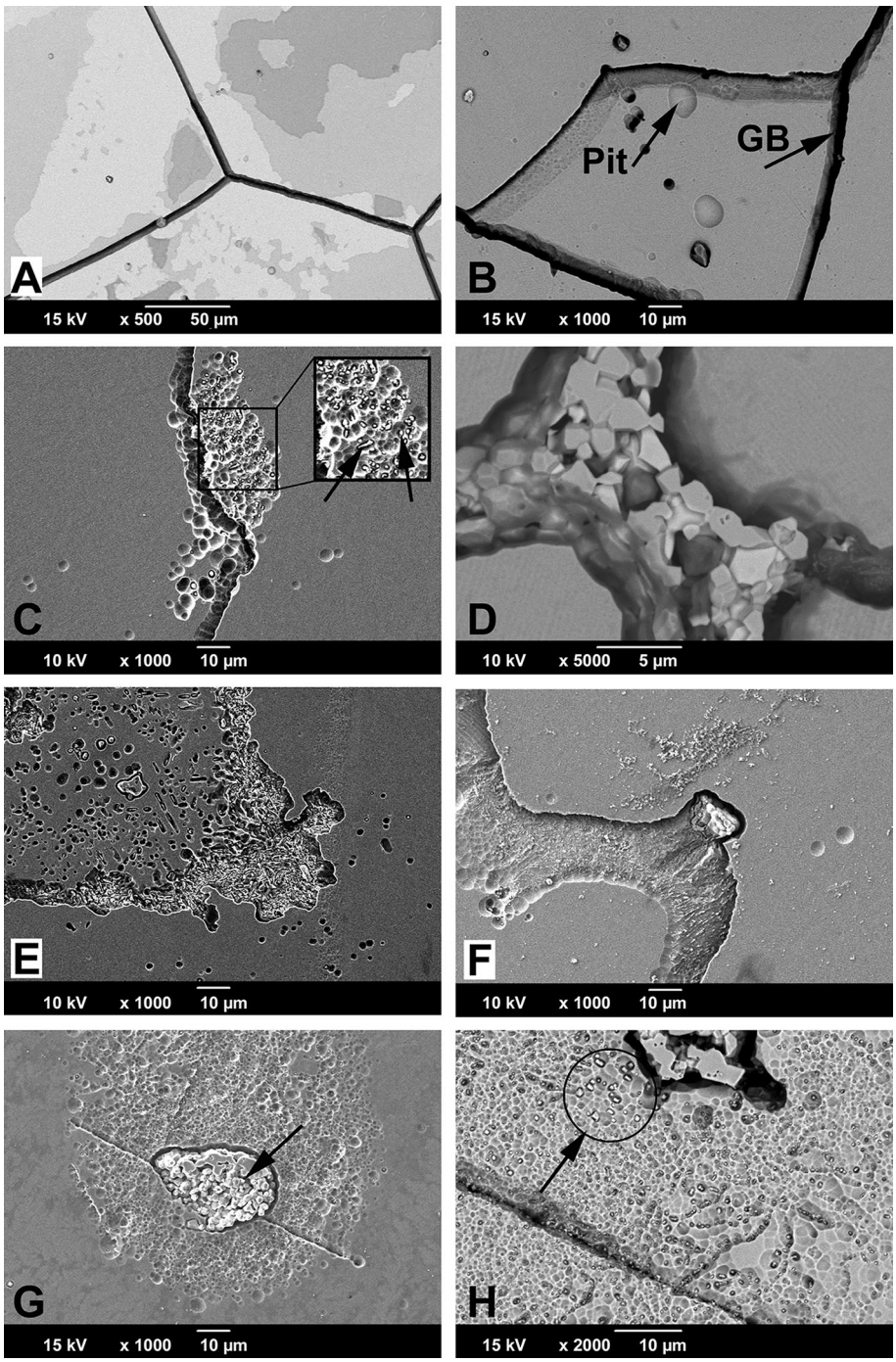
A
15 kV x 500 50 µm
B
Pit
GB
15 kV x 1000 10 µm
C
10 kV x 1000 10 µm
D
10 kV x 5000 5 µm
E
10 kV x 1000 10 µm
F
10 kV x 1000 10 µm
G
15 kV x 1000 10 µm
H
15 kV x 2000 10 µm

◀**Fig. 5A–H** SEM of damage features on cast alloy samples: (**A**, **B**) SA-1; (**C**–**F**) SA-2; and (**G**–**H**) SA-3. (**A**, **B**) SEM images of damage features of cast alloy SA-1 samples. SA-1 did not have hard phases. (**A**) Imaging with BSE mode revealed chromium oxide films on the surface along with grain boundary corrosion. Oxide films are visible because elements with low atomic numbers appear darker in BSE images. The actual alloy surface is the brightest area in the figure. Different shades of gray mark areas with oxide films that are thicker (> 0.5 μm) than the usual passive film (< 10 nm). Darker areas indicate thicker oxide films. (**B**) SA-1 sample with corrosion along the grain boundaries (GB) and a few random pits. (**C**) SA-2 sample showing pitting corrosion along grain boundaries in the presence of very fine hard phases (arrows). (**D**) BSE image of mixed hard phase along the grain boundary of a SA-2 sample: white phase (high atomic number) was rich in Mo and Si, gray phase exhibited mainly Co and Cr, and dark phases appeared to be carbides based on carbon content (low atomic number). (**E**) SA-2 sample showing small elongated and round pits that resulted from phase boundary corrosion and subsequent hard phase detachment. (**F**) SA-2 sample showing large shallow pit along a grain boundary that resulted from phase boundary corrosion and hard phase detachment. (**G**) SA-3 samples showing severe pitting around coarse hard phases. (**H**) SA-3 samples often exhibited fine hard phase clusters around coarse hard phases within grains that were associated with severe pitting. Fine hard phases appear bright using the BSE mode (arrow).

mean grain size (p = 0.11) with 5.6 μm (SD 0.9; 95% CI, 4.1–7.1), 4.1 μm (SD 1.5; 95% CI, 1.6–6.5), 4.2 μm (SD 1.2; 95% CI, 2.8–5.7), and 4.9 μm (SD 1; 95% CI, 0–13.8) for HA-1, HA-2, HA-3, and SA-4, respectively (Fig. 9A–D). There were also varying hard phase types and volume fractions. Some alloys had chromium carbides in a size range of 1–3 μm along with finer (< 1 μm) Mo- and Si-rich hard phases with varying volume fractions of < 1%–5% (Fig. 9A; Appendix 1), and others had no hard phases (Fig. 9B), but had more prominent crystallographic features such as twin boundaries or slip bands. Especially HA-3 samples exhibited a high concentration of slip bands with more distinct reliefs within individual grains after etching compared with other alloys (Fig. 9C). Other samples exhibited only a fine dispersion of Mo-rich hard phases without the presence of carbides or no hard phases at all (Fig. 9D; Appendix 1). For statistical comparison, alloys were distinguished between Type 1 wrought alloy with < 1% hard phases (Fig. 9E) and Type 2 wrought alloy with 1%–5% hard phase volume fraction (Fig. 9F). Based on the appearance of the alloy microstructure, it is likely that Type 1 was a low carbon alloy, and Type 2 was a high carbon alloy [3, 33]; however, this was not verified because the carbon content could not be quantified. After PDP tests, fine pitting could be observed for all alloys (Fig. 10). Those with hard phases exhibited phase boundary corrosion and pits formed after hard phase detachment, which was most notable for HA-1 samples (Fig. 10A). Unlike the head alloys, SA-4 exhibited pitting corrosion with a larger pit size (Fig. 10D). This alloy also appeared to have a low mean E_{corr} (−0.761 V, SD 0.001; 95% CI, −0.77 to -0.753) (Fig. 11A) and high mean I_{corr} (1.57×10^{-4} mA/cm^2, SD 3.39×10^{-5}; 95% CI, 1.33×10^{-4} to 4.62×10^{-4}) (Fig. 11B); however, the values could not be compared statistically with the head alloys as a result of the low number of available samples (N = 2). The head alloys had comparable values for E_{corr} and I_{corr} with −0.755 V (SD 0.006; 95% CI, −0.765 to −0.745), −0.757 V (SD 0.003; 95% CI, −0.762 to −0.753), and −0.756 V (SD 0.008;

Table 4. Mean values, SD, and 95% confidence interval (CI) for the corrosion potential (E_{corr}), corrosion current density (I_{corr}), and pitting potential (E_{pit}) for all components*

Sample number	E_{corr} (V versus SCE)			I_{corr} (mA/cm^2)			E_{pit} (V versus SCE)			Alloy category
	Mean	SD	95% CI	Mean	SD	95% CI	Mean	SD	95% CI	
SA-1	−0.751	0.005	−0.759 to −0.742	7.46×10^{-4}	1.37×10^{-4}	5.28×10^{-4} to 9.64×10^{-4}	0.505	0.035	0.450–0.561	Cast
SA-2	−0.755	0.004	−0.762 to −0.748	3.56×10^{-4}	2.73×10^{-4}	0−7.90×10^{-4}	0.469	0.027	0.425–0.512	Cast
SA-3	−0.755	0.005	−0.763 to −0.748	6.24×10^{-4}	4.69×10^{-4}	0−1.37×10^{-3}	0.486	0.080	0.359–0.613	Cast
SA-4	−0.761	0.001	−0.770 to −0.753	1.57×10^{-4}	3.39×10^{-5}	1.33×10^{-4} to 4.62×10^{-4}	0.636	0.000	0.632–0.640	Wrought
HA-1	−0.755	0.006	−0.765 to −0.745	9.72×10^{-5}	3.14×10^{-5}	4.72×10^{-5} to 1.47×10^{-4}	0.615	0.046	0.543–0.688	Wrought
HA-2	−0.757	0.003	−0.762 to −0.753	1.06×10^{-4}	2.95×10^{-5}	5.89×10^{-5} to 1.53×10^{-4}	0.681	0.032	0.629–0.732	Wrought
HA-3	−0.756	0.008	−0.766 to −0.747	1.04×10^{-4}	3.07×10^{-5}	6.59×10^{-5} to 1.42×10^{-4}	0.480	0.024	0.450–0.510	Wrought

* E_{corr} and E_{pit} are relative to the reference electrode (saturated calomel electrode [SCE]).

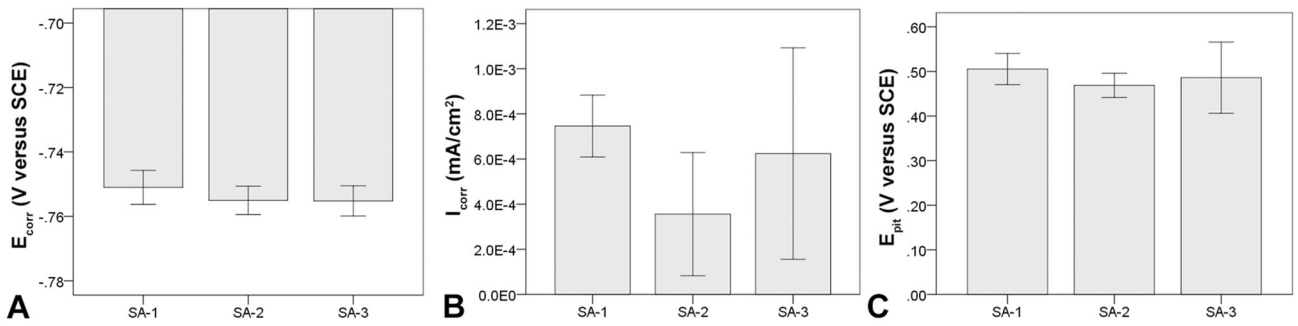

Fig. 6A–C Comparison of PDP metrics between different cast alloys. (**A**) E_{corr}, (**B**) I_{corr}, and (**C**) E_{pit} exhibited no difference but showed broad variability in some cases. All error bars represent SD.

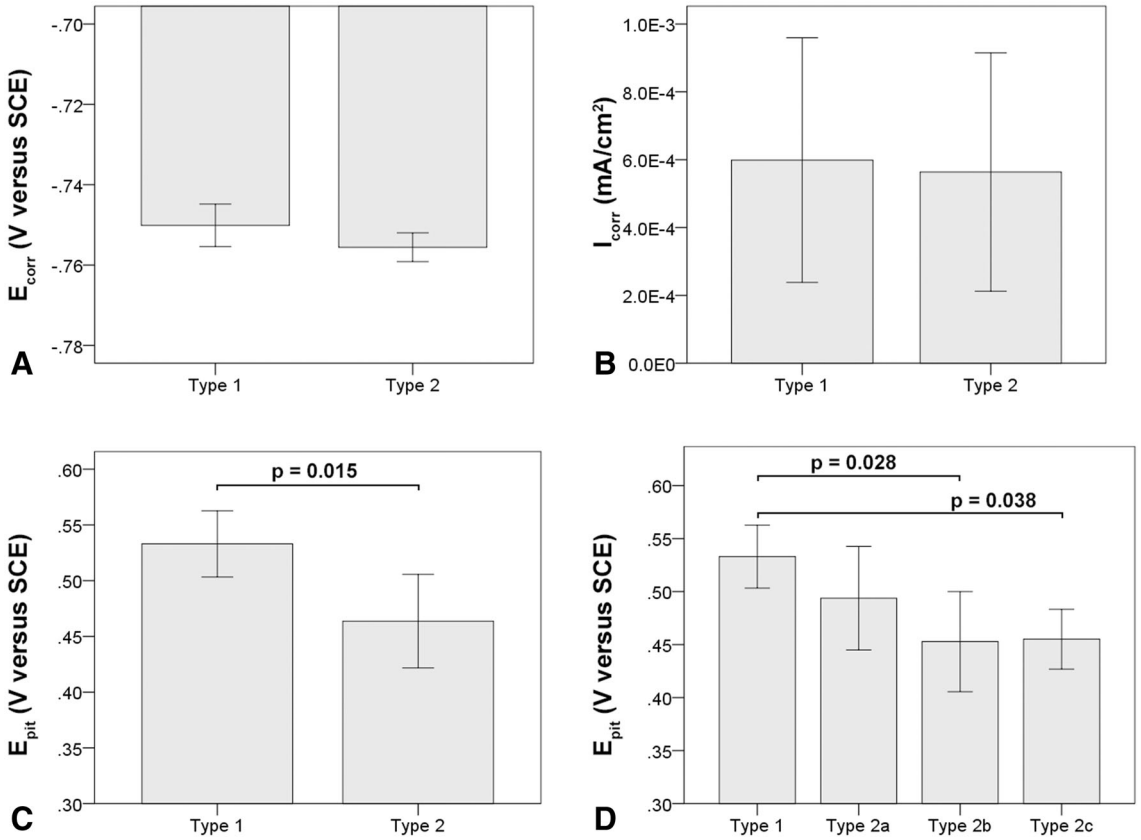

Fig. 7A–D Comparison of PDP metrics between cast alloy types without (Type 1) or with (Type 2) hard phases. (**A**) There was no difference in corrosion potential (E_{corr}) or (**B**) the corrosion current density (I_{corr}). (**C**) Cast alloys without hard phases (Type 1) had a more favorable E_{pit}. (**D**) Specifically, a difference was found between Type 1 alloy and subtypes 2b and 2c, but not 2a. The latter exhibited only few randomly distributed hard phases, whereas Type 2b exhibited numerous coarse and fine hard phases along grain boundaries, and Type 2c had coarse and fine hard phases within the grains. All error bars represent SD.

95% CI, −0.766 to −0.747) and 9.72×10^{-5} mA/cm^2 (SD 3.14×10^{-5}; 95% CI, 4.72×10^{-5} to 1.47×10^{-4}), 1.06×10^{-4} mA/cm^2 (SD 2.95×10^{-5}; 95% CI, 5.89×10^{-5} to 1.53×10^{-4}), and 1.04×10^{-4} mA/cm^2 (SD 3.07×10^{-5}; 95% CI, 6.59×10^{-5} to 1.42×10^{-4}) for HA-1, HA-2, and HA-3, respectively. There was no difference in E_{corr} and I_{corr} among all head alloys ($p = 0.66$, $p = 0.19$, respectively). The mean E_{pit} was 0.615 V (SD 0.046; 95% CI, 0.543–0.688), 0.681 V (SD 0.032; 95% CI, 0.629–0.732), and 0.480 V (SD 0.024; 95% CI, 0.45–0.51). HA-3 had a lower E_{pit} than HA-1 ($p = 0.005$) and HA-2 ($p < 0.001$) (Fig. 11C). By separating alloys with respect to hard phase

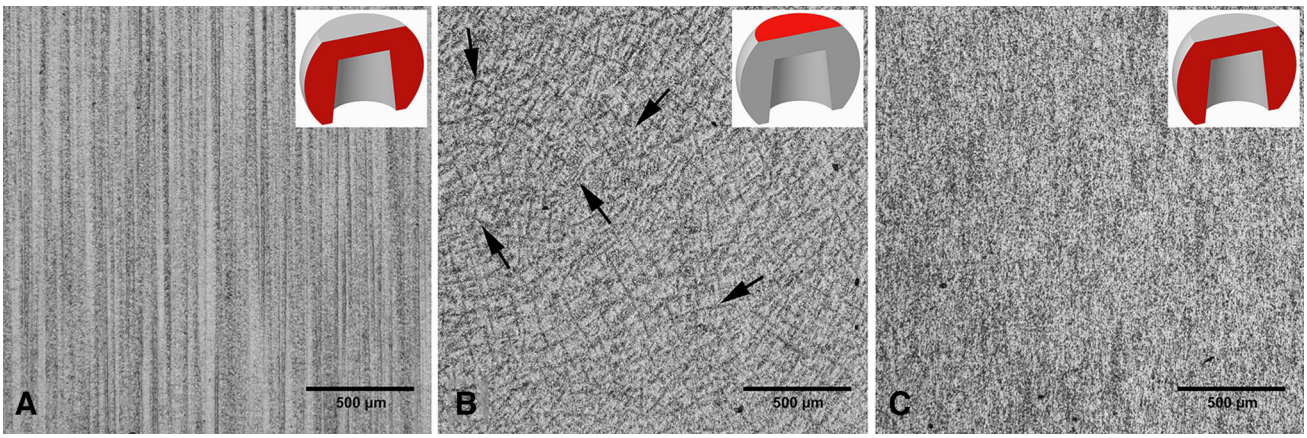

Fig. 8A–C Light micrographs showing typical examples of wrought alloy microstructure in (**A**) a longitudinal-oriented surface of a sample with banding, (**B**) a transverse-oriented surface of the same sample, and (**C**) a longitudinal-oriented surface of a sample, which did not show banding. (**A**) A banded structure running from the proximal to distal direction of the head is clearly exhibited. (**B**) In the transverse orientation, dendritic structures remain that were not removed during thermomechanical processing of the wrought alloy. Here, the residual dendritic structures are characterized by dark lines forming a distorted lattice structure (arrows). (**C**) No banding occurred in this alloy.

content, we observed the following values for Type 1 and Type 2, respectively: the E_{corr} was −0.761 V (SD 0.004; 95% CI, −0.766 to −0.757) and −0.756 (SD 0.005; 95% CI, −0.759 to −0.752), the I_{corr} was 1.28×10^{-4} mA/cm^2 (SD 1.31×10^{-5}; 95% CI, 1.12×10^{-4} to 1.44×10^{-4}) and 1.05×10^{-4} mA/cm^2 (SD 3.72×10^{-5}; 95% CI, 7.62×10^{-5} to 1.33×10^{-4}), and the E_{pit} was 0.592 V (SD 0.118; 95% CI, 0.445–0.739) and 0.604 V (SD 0.069; 95% CI, 0.551–0.657). E_{corr} was slightly higher ($p = 0.046$) for Type 2 compared with Type 1 alloy (Fig. 12A), whereas I_{corr} (Fig. 12B) and E_{pit} were similar ($p = 0.2$, $p = 0.82$, respectively). There was no difference in taper score ($p = 0.76$, Mann-Whitney U) between head tapers with Type 1 (median, 4.0; range, 1–4) or Type 2 (median, 4.0; range, 1–4) wrought alloy microstructure. As a result of the observation of the banded structure in the longitudinal direction, one sample out of each head alloy group (HA-1-1, HA-2-1, HA-3-1) was chosen to conduct PDP tests on transverse-oriented surfaces in addition to the longitudinal-oriented sample surfaces. The transverse-oriented samples had a mean E_{corr} of −0.731 V (SD 0.009; 95% CI, −0.752 to −0.709), I_{corr} of 5.2×10^{-5} (SD 2.6×10^{-5}; 95% CI, 0–1.16×10^{-4}), and E_{pit} of 0.49 V (SD 0.14; 95% CI, 0.145–0.834). The longitudinal-oriented samples had a median E_{corr} of −0.755 V (SD 0.003; 95% CI, −0762 to −0.748), I_{corr} of 1.14×10^{-5} (SD 1.47×10^{-5}; 95% CI, 7.69×10^{-5} to 1.5×10^{-4}), and E_{pit} of 0.659 V (SD 0.064; 95% CI, 0.5–0.82). The results showed that transverse-oriented sample surfaces had better corrosion behavior with respect to E_{corr} ($p = 0.008$) and I_{corr} ($p = 0.023$) than longitudinal-oriented surfaces (Fig. 12C–D), but there was no difference in E_{pit} ($p = 0.127$). The marked difference in E_{corr} and I_{corr} was independent of the manufacturer and hard phase content.

Discussion

Corrosion processes within modular taper junctions and subsequent ALTRs are a known cause of premature THA failure. It is important to eliminate or at least reduce the generation of corrosion products to prevent such implant failure. The cause of in vivo corrosion of metallic implants is multifactorial [1, 31]. It was the purpose of this study to identify differences in the corrosion behavior among different CoCrMo implant alloys and to determine how those differences may relate to the alloy microstructure. We made observations that support that a cast alloy microstructure is variable between manufacturers and dictates specific corrosion modes. Our results revealed not only fundamental differences in alloy microstructure among manufacturers or their suppliers, but also within single implant designs from the same manufacturer. Overall the cast alloy corrosion behavior appears to be linked to the presence of intermetallic hard phases and local inhomogeneity of the alloy's chemical composition. Furthermore, we found that microstructure of wrought alloys was more consistent between manufacturers or their suppliers with respect to grain size; however, it appeared that hard phases gave rise to phase boundary corrosion and subsequent local crevice corrosion. Most notable, we found that alloy segregations within wrought alloys had a strong negative impact on the corrosion behavior.

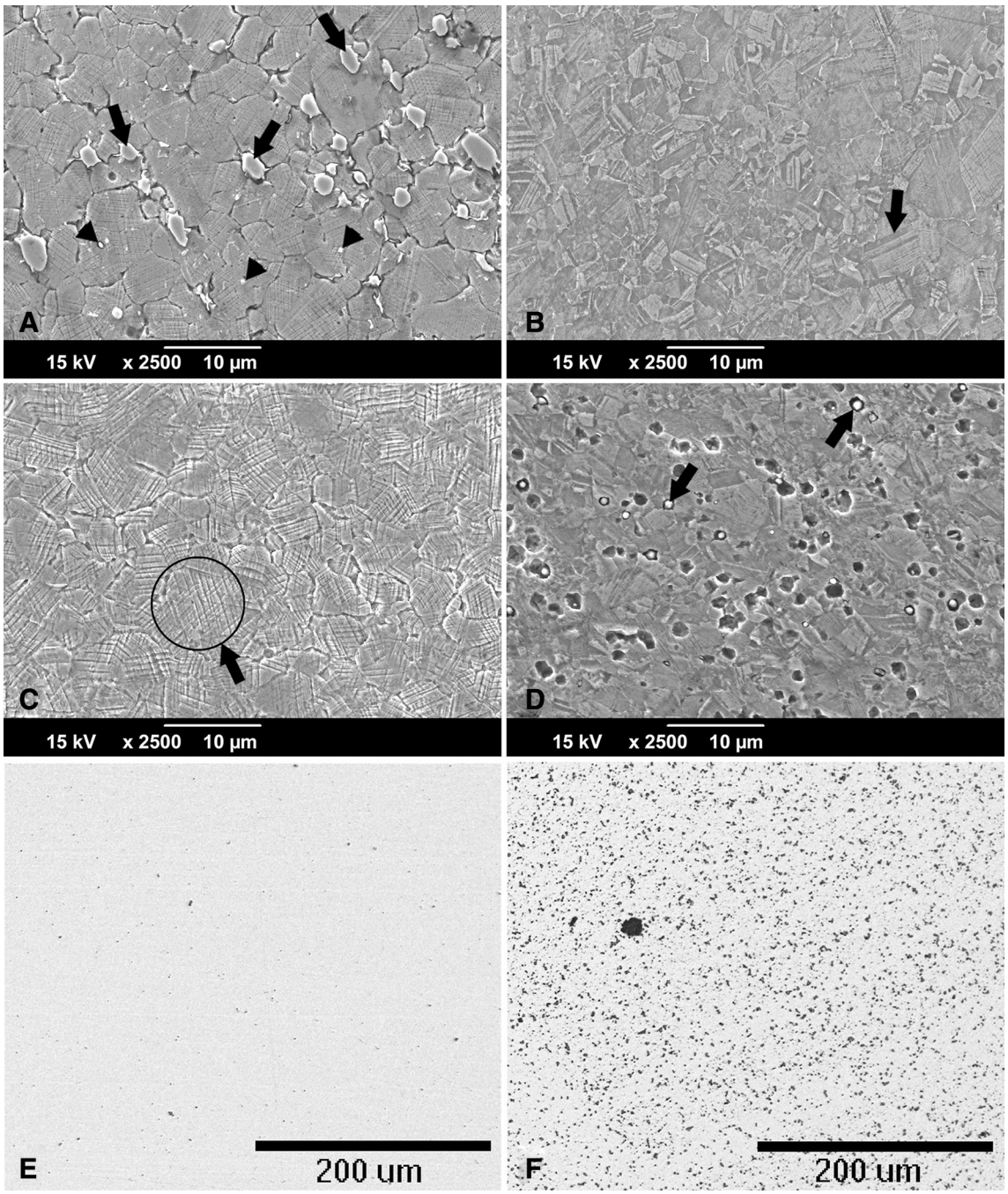

Fig. 9A–F Typical microstructure for all wrought alloys visualized through chemical etching: (**A**) HA-1: chromium carbides (arrows) and Mo-rich hard phases (arrow heads) are typically embedded within the matrix; (**B**) HA-2: typical grain structure with numerous twin boundaries (arrow); (**C**) HA-3: typical grain structure but with a high concentration of slip band reliefs (eg, as marked by arrow; (**D**) SA-4: fine grain size with fine Mo- and Si-rich hard phases embedded within the matrix (arrows) and some local pits presumably caused by hard phases detachment; (**E**) typical hard phase fraction (stained black) for Type 1 (< 1% hard phases) and (**F**) Type 2 (1%-5% hard phases) wrought alloy.

This study had several limitations. First, the total number of implants tested was not sufficient to determine consistent differences among manufacturers, especially considering the variation within each implant design. It also needs to be stated that it was unknown to the authors if some manufacturers had the same suppliers at different points in time. It is also possible that differences within a single design were the result of changes in the manufacturing process or location.

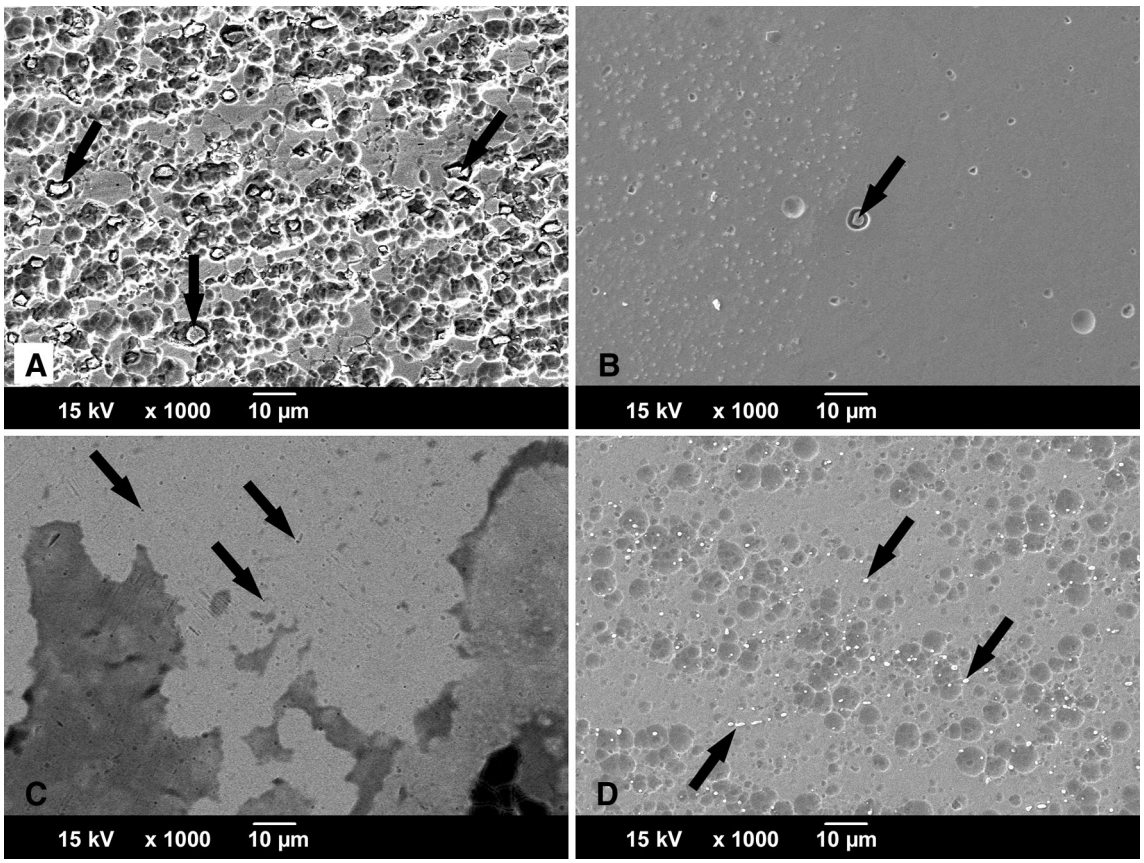

Fig. 10A–D SEM images of typically occurring damage features on wrought alloy surfaces after corrosion tests: (**A**) HA-1: numerous oddly shaped pits can be observed, which resulted from hard phase (predominantly carbide) detachment. Hard phases are still visible in some areas (arrows). (**B**) HA-2: random pits along with fine pits resulting from hard phase detachment and local phase boundary corrosion (arrow). (**C**) HA-3: very fine pits (arrows) and slight etching can be observed along with oxide films (gray areas) using the BSE mode. (**D**) SA-4: large round pits covering the entire surface in the presence of fine Mo- and Si-rich hard phases (arrows).

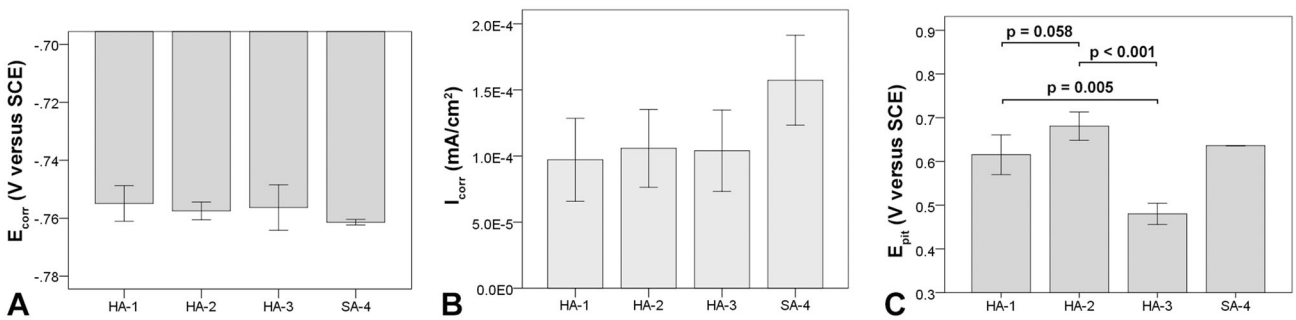

Fig. 11A–C The E_{corr} (**A**) and I_{corr} (**B**) were similar between all wrought alloys, but the E_{pit} (**C**) was markedly lower for HA-3 alloy. All error bars represent SD.

Another limitation lies in the use of cyclic PDP tests. PDP is an appropriate tool for the characterization of the electrochemical behavior of implant alloys; however, it does not simulate the in vivo processes of MACC. The test forces a potential loop on the sample that drives the surface from a cathodic potential through the passive regime, well into the transpassive regime and back within a few hours. This test cannot be directly compared with processes occurring over several years in vivo, yet the experiment enables us to compare basic electrochemical properties (Table 3) between alloys and furthermore exposes preferential sites of corrosive attacks—such as phase

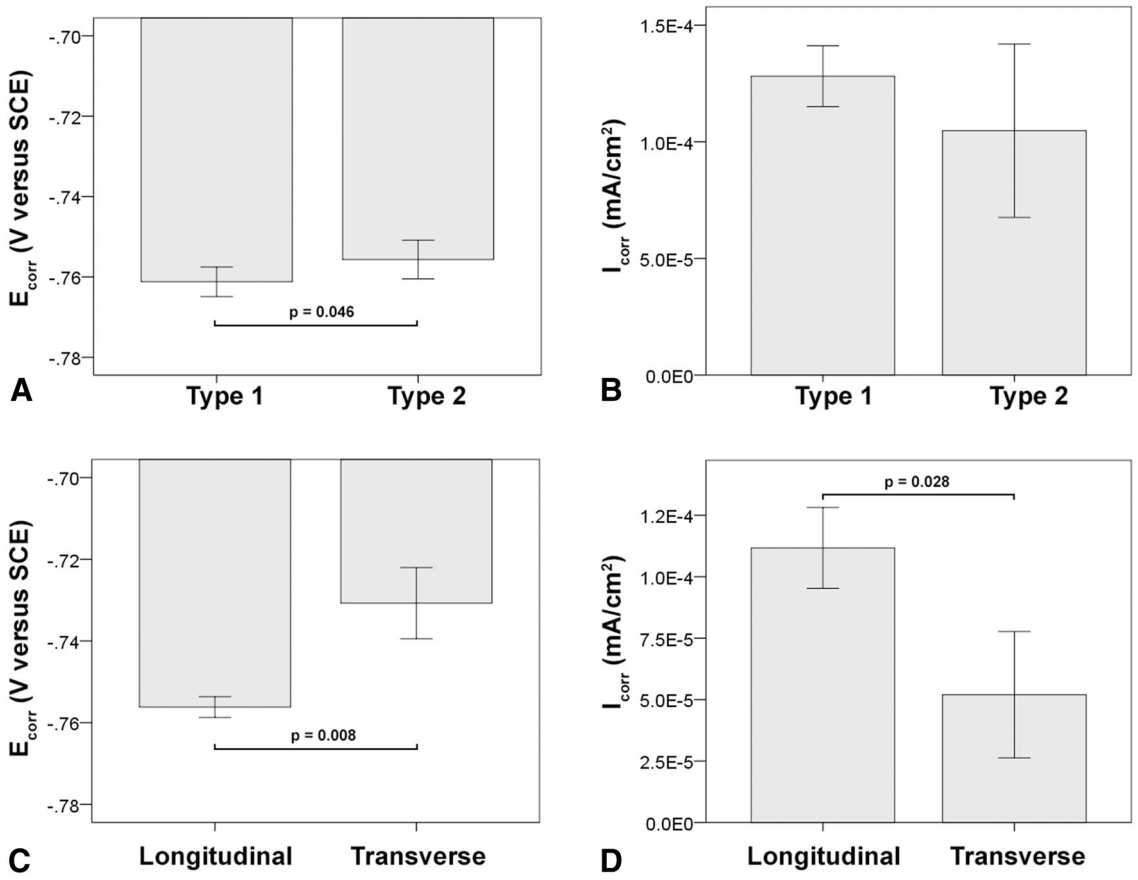

Fig. 12A–D Comparison of PDP metrics between wrought alloy with and without hard phases demonstrated slightly favorable E_{corr} (**A**), but similar I_{corr} (**B**) for samples with hard phases. With respect to sample surface orientation, transverse surfaces exhibited a more favorable E_{corr} (**C**) and I_{corr} (**D**) than longitudinal-oriented surfaces. All error bars represent SD.

boundaries—within the alloy microstructure and therefore was useful for the purpose of this study. However, it would be desirable to establish a testing protocol that mimics in vivo processes more closely. Lastly, it needs to be acknowledged that the characterization of implant alloy microstructural features was limited to the capabilities of the SEM and EDS system available for this study. Other tools such as high current field emission SEM, transmission electron microscopy, and electron diffraction pattern analysis would be useful to determine other microstructural features of a size below 500 nm. For example, it is possible that fine precipitates, hard phases, or impurities within the nanometer size range are present in the alloy that may help to further understand the observed corrosion behavior of the investigated alloys. Also, we were not able to determine the exact carbon content within each alloy with the available tools. In the case of wrought alloy, it is likely that Type 1 alloys had a low carbon content and Type 2 a high carbon content based on the presence of carbides [3, 33], but no definitive assessment could be made.

All cast alloy samples exhibited intergranular corrosion, but considerable pitting corrosion and phase boundary corrosion were only present in alloys with a considerable number of coarse hard phases or clusters of fine hard phases. Although intergranular corrosion has also been reported for wrought alloys in vitro [39], it appears to occur in vivo most frequently on cast alloy components (Fig. 1B) [15, 20]. It is not surprising that all three cast stem alloys (SA-1, SA-2, and SA-3) exhibited grain boundary corrosion, because grain boundaries are a common site of alloy inhomogeneity (eg, hard phase precipitation, accumulation of impurities) [39, 47]. There was good agreement among the electrochemical characterization, implant alloy microstructure, and the observed damage features. Pitting corrosion occurred primarily in areas around large hard phases and especially in areas with clusters of fine Mo- and Si-rich phases. It was not in the scope of this study to determine the hard phase structure. However, based on EDS measurements and SEM imaging with the BSE mode, comparisons can be drawn to previous work [42, 46]. Most hard phases were not carbides, but appeared to be some

type of intermetallic phase (eg, σ phase [24, 44]) as evidenced by the comparably low carbon peak and the presence of silicon [46]. It has been previously shown that such phases are likely to be intermetallic [24, 42, 46]. Intermetallic phases could be associated with a local imbalance of the chemical composition of the alloy [37, 42], which would align with the higher affinity to pitting corrosion observed in the SEM and the lower E_{pit} of those samples. The presence of coarse hard phases within the grain offers additional preferential corrosion sites leading to phase boundary corrosion. Both pitting and phase boundary corrosion are corrosion modes that can be observed on retrieved femoral stem tapers (Fig. 1A) [14, 19, 20]. The results of this study demonstrate that there were distinct differences regarding grain size and hard phase characteristics (size, type, volume fraction) among manufacturers, but also within each manufacturer. However, differences in the corrosion and pitting potential, E_{corr} and E_{pit}, were independent of the grain size and hard phase type and location and instead appeared to be driven by the total number of hard phases. Considering that most hard phases are intermetallic in nature, it is more likely that the corrosion behavior is only indirectly dependent on the presence of hard phases and that the enhanced pitting is instead a response to the inhomogeneous CoCrMo matrix surrounding those hard phases. However, further studies are needed to quantify the local alloy composition.

The wrought alloys appeared overall more similar among manufacturers than the cast alloys, but their corrosion behavior also appeared to be strongly dependent on microstructural features. A notable outlier was HA-3, which appeared to have a consistently higher lattice defect density throughout the bulk material as indicated by a prominent occurrence of slip bands. Such areas are more receptive to corrosion as a result of higher surface energy, which is reflected in the lower E_{pit}. The occurrence of such features is likely related to the thermomechanical treatment of the alloy. Different thermomechanical treatment parameters could reduce such residual features, but potentially also reduce the strength of the alloy. The dependency of E_{pit} on the hard phase content—as observed for the cast alloys—did not apply to the wrought alloys. This may be explained by the comparably higher homogeneity of the matrix and more uniform hard phase distribution, yet the observed damage features of the alloy samples with hard phases—likely to be high carbon alloy—exhibited oddly shaped pits, which were the result of phase boundary corrosion and subsequent hard phase detachment. Wrought alloys with a considerable hard phase volume fraction of $> 1\%$ exhibited severe damage features such as hard phase detachment followed by local crevice and grain boundary corrosion. Such a cascade of events can lead to excessive material loss within the modular junction as can be observed on the taper surface of HA-1-4, which was implanted for 9 years (Fig. 13). It is evident when comparing in vivo damage (Fig. 13) with the in vitro damage (Fig. 10A) of the same alloy that the initial phase boundary corrosion eventually led to complete grain dissolution. It needs to be discussed if hard phases—carbidic or intermetallic—are needed within the alloy. Historically, carbides were introduced to increase the hardness and wear resistance of the bearing surface in metal-on-metal THAs with mixed results [6, 9, 23, 49]. Their rationale for use in heads coupled with polyethylene cups or in femoral stems is unclear. Although the wrought alloy is more homogeneous than cast alloy, it is an important finding that almost all wrought alloy samples analyzed in this study exhibited a banded structure in the longitudinal direction. This finding is important because (1) alloys from all manufacturers were affected; (2) the head taper surface aligns with a deviation of only 2.83° from the longitudinally oriented banded microstructure; and (3) both the E_{corr} and the I_{corr} are unfavorable in this orientation. We have recently shown by EDS mapping that the banded microstructure was linked to areas of local molybdenum depletion [18]. This finding aligns well with the observed inferior corrosion behavior of surfaces with a banded microstructure, because molybdenum is known to enhance the stability of the alloy's protective passive film and thus the alloy's resistance to corrosion [12]. Furthermore, the banded structure appears to have the same orientation and geometry as the column-like damage pattern that has been observed in 35% of severely damaged femoral head retrievals [20]. Column-like damage was not observed in the two HA-1 alloys with a homogeneous microstructure in both longitudinal and transverse orientations (Table 2). Thus, it is likely that the mechanism behind the column-like damage feature is an etching process that exposed the banded microstructure and occurred repeatedly over time in vivo. The occurrence of the banded structure is indicative of the remains of former, slight segregations that were not fully removed during the thermomechanical treatment of the bar stock material. Interestingly, all three manufacturers of the head alloys were affected. It is also possible that the wrought stem alloy also exhibits a banded structure; however, the orientation of the stem taper axis in relation to the bar stock material is unknown.

It is important to note that there was no relationship between the Goldberg score and the alloy microstructure, yet the microstructure had clear implications on the corrosion modes. Therefore, it seems likely that specific microstructural characteristics can make a cast or wrought CoCrMo alloy only more or less prone to some corrosion modes. There still must be other contributing factors such as micromotion, taper angular mismatch, surface topography, assembly load, and synovial fluid composition that

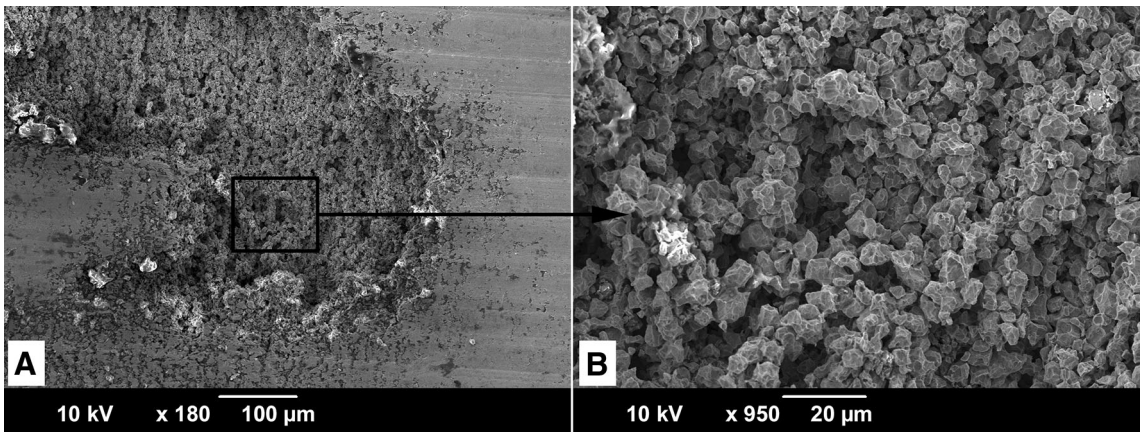

Fig. 13A–B (**A**) Severe in vivo corrosion damage on the taper surface corresponding to HA-1-4; (**B**) at higher magnification, the complete dissolution of the grain structure can be seen.

initially enable the process of MACC [25, 31, 41, 43]. For example, fretting and imprinting processes may lead to widening of the crevices allowing joint fluid to enter and potentially change the chemical environment. The exact pathways leading to the harsh electrochemical environment that enables the observed corrosion modes are yet unclear. High potentials (as applied during PDP) and low pH (as applied during laboratory etching) seem unlikely to occur in vivo, yet these appear to be the only processes that would explain the close resemblance of our laboratory and retrieval findings. Another possible explanation may be related to the release of highly reactive oxygen species released during cellular activity in the joint environment [16]. Further investigations are warranted to determine how such potentially inflammatory processes could generate the environmental conditions needed to cause the observed damage on CoCrMo alloy surfaces within modular taper junctions. However, based on our results, it appears that certain microstructural features can make the alloy more or less vulnerable to corrosion under those chemical conditions.

In conclusion, we found considerable variability in alloy microstructure of cast and wrought CoCrMo alloys, all of which conform to ASTM standards. Microstructural features such as hard phase type and location, residual alloy segregation, and lattice defect accumulation appear to dictate corrosion modes such as etching, phase boundary corrosion, pitting corrosion, and column damage that have been frequently observed on retrievals by our laboratory and others [14, 19, 20]. The occurrence of such corrosion modes can be expected to have a meaningful impact on the emission of metal ions and other corrosion products, potentially increasing the risk of ALTRs. However, our findings suggest that an alloy with a minimum number of hard phases and a homogeneous CoCrMo matrix may reduce susceptibility to corrosion and metal ion release, which could be clinically beneficial.

Acknowledgments We thank Luis F. Simoes (Federal University of Itajuba, Brazil), Jennifer Wright, Dr Hannah Lundberg, Dr Dmitry Royhman (Rush University Medical Center, Chicago, IL, USA), and Dr Alfons Fischer (University of Duisburg-Essen, Germany) for their support, advice, and productive discussions.

References

1. Arnholt C, Underwood R, MacDonald DW, Higgs GB, Chen AF, Klein G, Hamlin B, Lee G-C, Mont M, Cates H, Malkani A, Kraay M, Rimnac C, Kurtz SM. Microgrooved surface topography does not influence fretting corrosion of tapers in total hip arthroplasty: classification and retrieval analysis. In: Greenwald AS, Kurtz SM, Lemons JE, Mihalko WM, eds. *Modularity and Tapers in Total Joint Replacement Devices. ASTM STP1591*. West Conshohocken, PA, USA: ASTM International; 2015:99–112.
2. ASTM F75-12. *Standard Specification for Cobalt-28 Chromium-6 Molybdenum Alloy Castings and Casting Alloy for Surgical Implants*. West Conshohocken, PA, USA: ASTM International; 2012.
3. ASTM F1537-11. *Standard Specification for Wrought Cobalt-28Chromium-6Molybdenum Alloys for Surgical Implants*. West Conshohocken, PA, USA: ASTM International, USA; 2011.
4. Berry G, Bolton J, Brown J, McQuaide S. The production and properties of wrought high carbon Co-Cr-Mo alloys. In: Disegi JE, Kennedy RL, Pilliar R, eds. *Cobalt-base Alloys for Biomedical Applications. ASTM STP 1365*. West Conshohocken, PA, USA: ASTM International; 1999:11–31.
5. Bishop N, Witt F, Pourzal R, Fischer A, Rütschi M, Michel M, Morlock M. Wear patterns of taper connections in retrieved large diameter metal-on-metal bearings. *J Orthop Res.* 2013;31:1116–1122.
6. Bowsher JG, Nevelos J, Williams PA, Shelton JC. 'Severe' wear challenge to 'as-cast' and 'double heat-treated' large-diameter metal-on-metal hip bearings. *Proc Inst Mech Eng [H].* 2006;220:135–143.
7. Brown SA, Flemming CA, Kawalec JS, Placko HE, Vassaux C, Merritt K, Payer JH, Kraay MJ. Fretting corrosion accelerates

crevice corrosion of modular hip tapers. *J Appl Biomater.* 1995;6:19–26.
8. Catelas I, Petit A, Zukor DJ, Huk OL. Cytotoxic and apoptotic effects of cobalt and chromium ions on J774 macrophages—implication of caspase-3 in the apoptotic pathway. *J Mater Sci Mater Med.* 2001;12:949–953.
9. Chiba A, Kumagai K, Nomura N, Miyakawa S. Pin-on-disk wear behavior in a like-on-like configuration in a biological environment of high carbon cast and low carbon forged Co-29Cr-6Mo alloys. *Acta Mater.* 2007;55:1309–1318.
10. Cook RB, Bolland BJRF, Wharton JA, Tilley S, Latham JM, Wood RJK. Pseudotumour formation due to tribocorrosion at the taper interface of large diameter metal on polymer modular total hip replacements. *J Arthroplasty*. 2013;28:1430–1436.
11. Cooper HJ, Della Valle CJ, Berger RA, Tetreault M, Paprosky WG, Sporer SM, Jacobs JJ. Corrosion at the head-neck taper as a cause for adverse local tissue reactions after total hip arthroplasty. *J Bone Joint Surg Am.* 2012;94:1655–1661.
12. Devine TM, Wulff J. The comparative crevice corrosion resistance of Co-Cr base surgical implant alloys. *J Electrochem Soc.* 1976;123:1433–1437.
13. Fischer A, Janssen D, Wimmer MA. The influence of molybdenum on the fretting corrosion behavior of CoCr/TiAlV Couples. *Biotribology*. Available at: http://www.sciencedirect.com/science/article/pii/S2352573816300555. Accessed May 30, 2017.
14. Gilbert JL, Buckley CA, Jacobs JJ. In vivo corrosion of modular hip prosthesis components in mixed and similar metal combinations. The effect of crevice, stress, motion, and alloy coupling. *J Biomed Mater Res.* 1993;27:1533–1544.
15. Gilbert JL, Buckley CA, Jacobs JJ, Bertin KC, Zernich MR. Intergranular corrosion-fatigue failure of cobalt-alloy femoral stems. A failure analysis of two implants. *J Bone Joint Surg Am.* 1994;76:110–115.
16. Gilbert JL, Sivan S, Liu Y, Kocagöz SB, Arnholt CM, Kurtz SM. Direct in vivo inflammatory cell-induced corrosion of CoCrMo alloy orthopedic implant surfaces. *J Biomed Mater Res A*. 2015;103:211–223.
17. Goldberg JR, Gilbert JL, Jacobs JJ, Bauer TW, Paprosky W, Leurgans S. A multicenter retrieval study of the taper interfaces of modular hip prostheses. *Clin Orthop Relat Res.* 2002;401:149–161.
18. Hall DJ, McCarthy SM, Ehrich J, Urban RM, Fischer A, Lundberg HJ, Jacobs JJ, Pourzal R. Imprinting and column damage on CoCrMo head taper surfaces in total hip replacements. In: Mihalko WM, Lemons JE, Greenwald AS, Kurtz SM, eds. *Symposium on Beyond the Implant: Retrieval Analysis Methods for Implant Surveillance*. *STP1606*. West Conshohocken, PA, USA: ASTM International; 2017.
19. Hall DJ, Pourzal R, Della Valle CJ, Galante JO, Jacobs JJ, Urban RM. *Corrosion of Modular Junctions in Femoral and Acetabular Components for Hip Arthroplasty and Its Local and Systemic Effects.* West Conshohocken, PA, USA: ASTM International; 2015:420–427.
20. Hall DJ, Pourzal R, Lundberg HJ, Mathew MT, Jacobs JJ, Urban RM. Mechanical, chemical and biological damage modes within head-neck tapers of CoCrMo and Ti6Al4 contemporary hip replacements. *J Biomed Mater Res B Appl Biomater.* 2017 Aug 26. [Epub ahead of print]
21. Hothi HS, Matthies AK, Berber R, Whittaker RK, Skinner JA, Hart AJ. The reliability of a scoring system for corrosion and fretting, and its relationship to material loss of tapered, modular junctions of retrieved hip implants. *J Arthroplasty*. 2014;29:1313–1317.
22. Jacobs JJ, Gilbert JL, Urban RM. Current concepts review—corrosion of metal orthopaedic implants. *J Bone Joint Surg Am.* 1998;80:268–282.
23. Kamali A, Hussain A, Li C, Pamu J, Daniel J, Ziaee H, McMinn DJW. Tribological performance of various CoCr microstructures in metal-on-metal bearings: the development of a more physiological protocol in vitro. *J Bone Joint Surg Br.* 2010;92:717.
24. Kilner T, Pilliar R, Weatherly G, Allibert C. Phase identification and incipient melting in a cast Co-Cr surgical implant alloy. *J Biomed Mater Res.* 1982;16:63–79.
25. Kocagöz SB, Underwood RJ, Sivan S, Gilbert JL, MacDonald DW, Day JS, Kurtz SM. Does taper angle clearance influence fretting and corrosion damage at the head–stem interface? A matched cohort retrieval study. *Semin Arthroplasty*. 2013;24:246–254.
26. Kurtz SM, Ong KL, Lau E, Bozic KJ. Impact of the economic downturn on total joint replacement demand in the United States: updated projections to 2021. *J Bone Joint Surg Am.* 2014;96:624–630.
27. Kwon YM, Xia Z, Glyn-Jones S, Beard D, Gill HS, Murray DW. Dose-dependent cytotoxicity of clinically relevant cobalt nanoparticles and ions on macrophages in vitro. *Biomed Mater.* 2009;4:025018.
28. Liao Y, Pourzal R, Stemmer P, Wimmer MA, Jacobs JJ, Fischer A, Marks LD. New insights into hard phases of CoCrMo metal-on-metal hip replacements. *J Mech Behav Biomed Mater.* 2012;12:39–49.
29. Lindgren JU, Brismar BH, Wikstrom AC. Adverse reaction to metal release from a modular metal-on-polyethylene hip prosthesis. *J Bone Joint Surg Br.* 2011;93:1427–1430.
30. Lippard HE, Kennedy RL. Process metallurgy of wrought CoCrMo alloy. In: Disegi JE, Kennedy RL, Pilliar R, eds. *Cobalt-base Alloys for Biomedical Applications*. *ASTM STP 1365.* West Conshohocken, PA, USA: ASTM International; 1999:98–107.
31. Lundberg HJ, Ha NQ, Hall DJ, Urban RM, Levine BR, Pourzal R. *Contact Mechanics and Plastic Deformation at the Local Surface Topography Level After Assembly of Modular Head-neck Junctions in Modern Total Hip Replacement Devices. STP1591.* West Conshohocken, PA, USA: ASTM International; 2015:59–82.
32. Mathew MT, Jacobs JJ, Wimmer MA. Wear-corrosion synergism in a CoCrMo hip bearing alloy is influenced by proteins. *Clin Orthop Relat Res.* 2012;470:3109–3117.
33. Mathew MT, Nagelli C, Pourzal R, Fischer A, Laurent MP, Jacobs JJ, Wimmer MA. Tribolayer formation in a metal-on-metal (MoM) hip joint: an electrochemical investigation. *J Mech Behav Biomed Mater.* 2014;29:199–212.
34. Mathew MT, Runa MJ, Laurent M, Jacobs JJ, Rocha LA, Wimmer MA. Tribocorrosion behavior of CoCrMo alloy for hip prosthesis as a function of loads: a comparison between two testing systems. *Wear*. 2011;271:1210–1219.
35. McGrory BJ, MacKenzie J, Babikian G. A high prevalence of corrosion at the head–neck taper with contemporary Zimmer non-cemented femoral hip components. *J Arthroplasty*. 2015;30:1265–1268.
36. McMinn D, Daniel J. History and modern concepts in surface replacement. *Proc Inst Mech Eng [H].* 2006;220:239–251.
37. Mishra AK, Hamby MA, Kaiser WB. Metallurgy, microstructure, chemistry and mechanical properties of a new grade of cobalt-chromium alloy before and after porous coating. In: Disegi JE, Kennedy RL, Pilliar R, eds. *Cobalt-base Alloys for Biomedical Applications*. *ASTM STP 1365.* West Conshohocken, PA, USA: ASTM International; 1999:71–88.
38. Nganbe M, Khan U, Louati H, Speirs A, Beaulé PE. In vitro assessment of strength, fatigue durability, and disassembly of Ti6Al4V and CoCrMo necks in modular total hip replacements. *J Biomed Mater Res B Appl Biomater.* 2011;97B:132–138.
39. Panigrahi P, Liao Y, Mathew MT, Fischer A, Wimmer MA, Jacobs JJ, Marks LD. Intergranular pitting corrosion of CoCrMo

biomedical implant alloy. *J Biomed Mater Res Part B Appl Biomater.* 2014;102:850–859.
40. Plummer DR, Berger RA, Paprosky WG, Sporer SM, Jacobs JJ, Della Valle CJ. Diagnosis and management of adverse local tissue reactions secondary to corrosion at the head-neck junction in patients with metal on polyethylene bearings. *J Arthroplasty*. 2016;31:264–268.
41. Porter DA, Urban RM, Jacobs JJ, Gilbert JL, Rodriguez JA, Cooper HJ. Modern trunnions are more flexible: a mechanical analysis of THA taper designs. *Clin Orthop Relat Res.* 2014;472:3963–70.
42. Pourzal R. Possible pathways of particle formation in CoCrMo sliding wear. *Fortschr.-Berichte VDI*. Duesseldorf, Germany: VDI Verlag; 2012;Reihe 17, No. 285.
43. Pourzal R, Hall DJ, Ha NQ, Urban RM, Levine BR, Jacobs JJ, Lundberg HJ. Does surface topography play a role in taper damage in head-neck modular junctions? *Clin Orthop Relat Res.* 2016;474:2232–2242.
44. Rajan K. Thermodynamic assessment of heat treatments for a Co-Cr-Mo alloy. *J Mater Sci.* 1983;18:257–264.
45. Scully WF, Teeny SM. Pseudotumor associated with metal-on-polyethylene total hip arthroplasty. *Orthopedics*. 2013;36:e666–670.
46. Stemmer P, Pourzal R, Liao Y, Marks L, Morlock M, Jacobs JJ, Wimmer MA, Fischer A. Microstructure of retrievals made from standard cast HC-CoCrMo alloys. In: Kurtz SM, Greenwald AS, Mihalko WH, Lemons JE, eds. *Metal-on-metal Total Hip Replacement Devices*. West Conshohocken, PA, USA: ASTM International; 2013:251–267.
47. Tandon R. Net shaping of Co-Cr-Mo (F-75) via metal injection molding. In: Disegi JE, Kennedy RL, Pilliar R, eds. *Cobalt-base Alloys for Biomedical Applications*. *ASTM STP 1365.* West Conshohocken, PA, USA: ASTM International; 1999:3–10.
48. Van Citters DW, Martin AJ, Currier JH, Park S-H, Edidin AA. Factors related to imprinting corrosion in modular head-neck junctions. In: Greenwald AS, Kurtz SM, Lemons JE, Mihalko WM, eds. *Modularity and Tapers in Total Joint Replacement Devices*. *STP 1591*. West Conshohocken, PA, USA: ASTM International; 2015:83–98.
49. Varano R, Bobyn JD, Medley JB, Yue S. The effect of microstructure on the wear of cobalt-based alloys used in metal-on-metal hip implants. *Proc Inst Mech Eng [H]*. 2006;220:145–159.
50. Whitehouse MR, Endo M, Masri BA. Adverse local tissue reaction associated with a modular hip hemiarthroplasty. *Clin Orthop Relat Res.* 2013;471:4082–4086.